ELSEVIER

Volume 180, Number 8, August 2007

JOURNAL OF SOLID STATE CHEMISTRY

www.elsevier.com/locate/jssc

CONTENTS

Abstracted/indexed in BioEngineering Abstracts, Chemical Abstracts, Coal Abstracts, Current Contents/Physics, Chemical, & Earth Sciences, Engineering Index, Research Alert, SCISEARCH, Science Abstracts, and Science Citation Index. Also covered in the abstract and citation database SCOPUS®. Full text available on ScienceDirect®.

Regular Articles

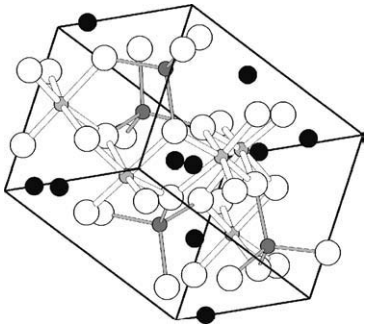

Structure of $LiMnNbO_4$: ball-and-stick model of the unit cell (Li–O bonds are not shown, Mn–O bonds are gray, Nb–O bonds are white).

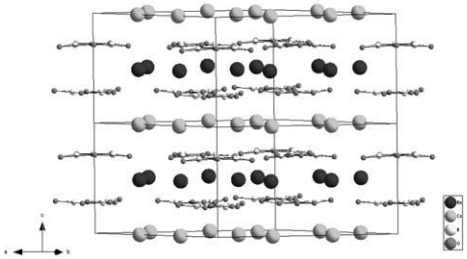

A new ternary borate oxide, cesium barium borate, $CsBaB_3O_6$ has been synthesized. The structure can be viewed as layer-like structure, which is made up of B_3O_6 plane hexagonal rings stacking along the *c*-axis, with the Cs and Ba atoms alternately occupying sites between the B_3O_6 sheets.

Regular Articles—Continued

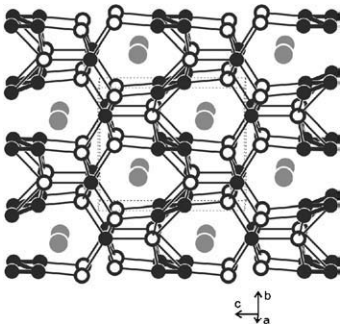

The three-dimensional $[Au_3In_3]$ network in $SrAu_3In_3$.

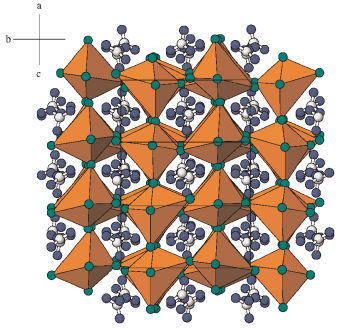

The perovskite-like crystals of $C(NH_2)_3SnCl_3$ undergo two successive first-order phase transitions at 400 and 419 K, both accompanied by an essential order–disorder contribution. The *p–T* phase diagram exhibits a singular point at 219 MPa and 443 K.

Ternary rare-earth titanium antimonides: Phase equilibria in the *RE*–Ti–Sb (*RE* = La, Er) systems and crystal structures of $RE_2Ti_7Sb_{12}$ (*RE* = La, Ce, Pr, Nd) and $RETi_3(Sn_xSb_{1-x})_4$ (*RE* = Nd, Sm)

Haiying Bie, S.H. Devon Moore, Davin G. Piercey, Andriy V. Tkachuk, Oksana Ya. Zelinska and Arthur Mar

Page 2216

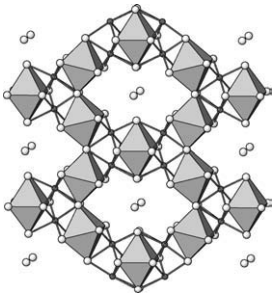

$La_2Ti_7Sb_{12}$ contains sectioned layers consisting of Ti-centred octahedra linked by corner- and face-sharing.

Synthesis and structure of a 1,6-hexyldiamine heptaborate, $[H_3N(CH_2)_6NH_3][B_7O_{10}(OH)_3]$

Sihai Yang, Guobao Li, Shujian Tian, Fuhui Liao, Ming Xiong and Jianhua Lin

Page 2225

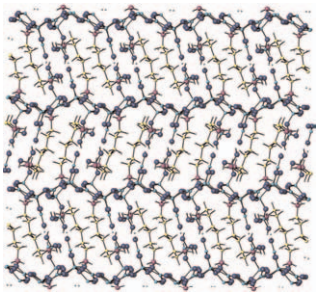

A layered 1,6-hexyldiamine heptaborate, $[H_3N(CH_2)_6NH_3][B_7O_{10}(OH)_3]$, was solvothermally synthesized at 150 °C. It is a layer borate and crystallized in monoclinic space group $P2_1/n$ with $a = 8.042(2)$ Å, $b = 20.004(4)$ Å, $c = 10.103(2)$ Å, $\beta = 90.42(3)°$.

Orthorhombic superstructures within the rare earth strontium-doped cobaltate perovskites: $Ln_{1-x}Sr_xCoO_{3-\delta}$ ($Ln = Y^{3+}$, Dy^{3+}–Yb^{3+}; $0.750 \leqslant x \leqslant 0.875$)

Michael James, Maxim Avdeev, Paris Barnes, Liliana Morales, Kia Wallwork and Ray Withers

Page 2233

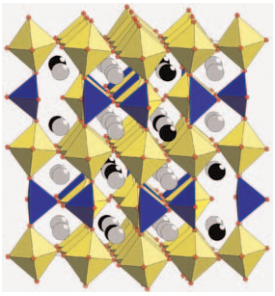

A study using electron, high-resolution synchrotron X-ray and neutron powder diffraction reveals a new family of orthorhombic perovskite superstructures ($Ln_{0.2}Sr_{0.8}CoO_{3-\delta}$), that shows A-site ($Ln^{3+}/Sr^{2+}$) cation ordering as well as oxygen vacancy ordering.

Crystal structure and phase transitions of Sr_2CdWO_6

M. Gateshki, J.M. Igartua and A. Faik

Page 2248

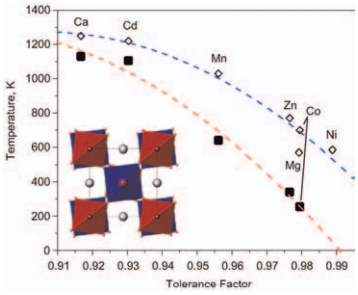

The phase transition temperatures as a function of the tolerance factor *t*, calculated using bond lengths distances that give the nominal oxidation states of the cations in the bond–valence method. The phase transition temperatures increase at lower values of *t*. Also, the temperature range in which the tetragonal phase exists is narrower at low *t*. These results are very similar to those observed in Rb_2KBF_2(B = Sc, In, Lu, Er, Ho) elpasolites, and confirm that the most important factor governing the appearance of octahedral tilts in the double perovskite structure and the temperature range in which they exist is the mismatch between the size of the A cation and interstitial space between the BO_6 and $B'O_6$ octahedra.

A new structure type of phosphate: Crystal structure of $Na_2Zn_5(PO_4)_4$

L.N. Ji, H.W. Ma, J.B. Li, J.K. Liang, B.J. Sun, Y.H. Liu, J.Y. Zhang and G.H. Rao

Page 2256

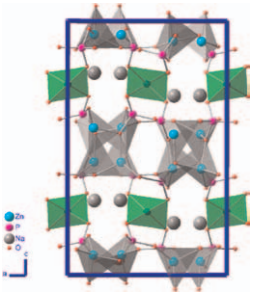

Crystal structure and the relevant properties of $Na_2Zn_5(PO_4)_4$, the first zincophosphate which having 3D $[Zn_5P_4O_{16}]_n^{2n-}$ covalent framework and the lowest P/Zn atomic ratio, were reported. The powder diffraction pattern of $Na_9Zn_{21}(PO_4)_{17}$ was proved to be a mixture of $Na_2Zn_5(PO_4)_4$ and $NaZnPO_4$ in the molar ratio of 4:1 by Rietveld refinement.

Synthesis and characterization of silver nanowires with zigzag morphology in *N*,*N*-dimethylformamide

Xin He, Xiujian Zhao, Yunxia Chen, Jinyang Feng and Zhenya Sun

Page 2262

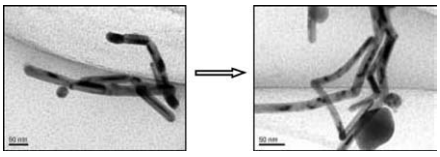

The evolution process of zigzag silver nanowires developed from the end-to-end assemblies of silver nanorods.

Continued

Synthesis and green up-conversion fluorescence of colloidal $La_{0.78}Yb_{0.20}Er_{0.02}F_3/SiO_2$ core/shell nanocrystals
Yan Wang, Weiping Qin, Jisen Zhang, Chunyan Cao, Jishuang Zhang, Ye Jin, Peifen Zhu, Guodong Wei, Guofeng Wang and Lili Wang
Page 2268

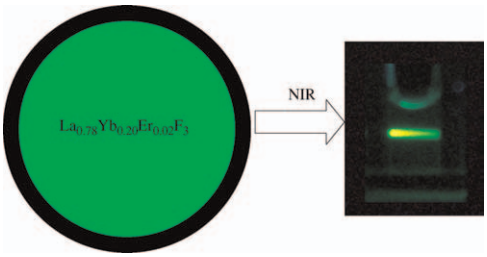

Colloidal $La_{0.78}Yb_{0.20}Er_{0.02}F_3/SiO_2$ Core/Shell nanocrystals (NCs) were synthesized and the free amino groups were introduced to the surface of silica shells by copolymerization 3-aminopropyl (triethoxy)silane. The NCs can be dispersed in ethanol and water to form stable colloidal solution. In addition, the NCs exhibit green up-conversion fluorescence under 980-nm excitation.

Covalent modification of calcium hydroxyapatite surface by grafting phenyl phosphonate moieties
Abdallah Aissa, Mongi Debbabi, Michel Gruselle, René Thouvenot, Patrick Gredin, Rainer Traksmaa and Kaia Tõnsuaadu
Page 2273

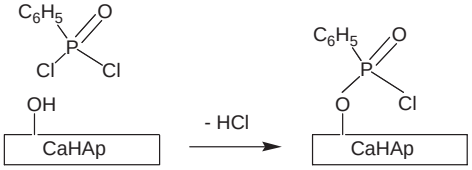

Representation of the first step of the reaction between the phenyl phosphonic dichloride and the hydroxyl groups on the surface of the apatite, leading to covalent P–O–P bond with elimination of HCl.

Characterization of homoionic Fe^{2+}-type montmorillonite: Potential chemical species of iron contaminant
Naofumi Kozai, Koichi Inada, Yoshifusa Adachi, Sachi Kawamura, Yusuke Kashimoto, Tamotsu Kozaki, Seichi Sato, Toshihiko Ohnuki, Takuro Sakai, Takahiro Sato, Masakazu Oikawa, Fumitaka Esaka and Hisayoshi Mitamura
Page 2279

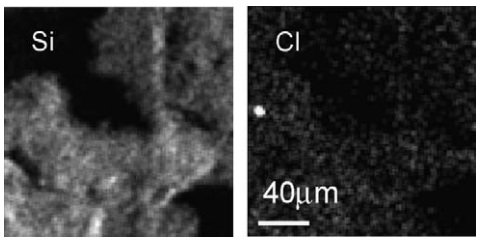

The distribution of Si (left) and Cl (right) in homoionic Fe^{2+}-type montmorillonite prepared under an inert gas atmosphere by a conventional method using a $FeCl_2$ solution. A small fraction of chloride ions remained dispersed throughout the clay. This paper mainly discusses the potential contaminant iron chemical species in this sample other than Fe^{2+} ions.

Sol–gel synthesis of hydrous ruthenium oxide nanonetworks from 1,2-epoxides
Jeremy Walker, R. Bruce King and Rina Tannenbaum
Page 2290

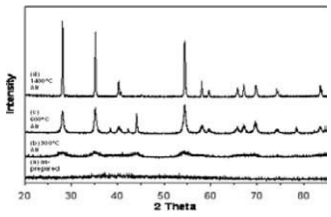

Heating of hydrous ruthenium oxide, $RuO_2 \cdot xH_2O$, under an inert atmosphere, results in its complete reduction to the zero-valent state, whereas heating it in air results in both crystalline anhydrous RuO_2 and zero-valent ruthenium, depending on the method of heating.

Electron-poor $SrAu_xIn_{4-x}$ ($0.5 \leqslant x \leqslant 1.2$) and $SrAu_xSn_{4-x}$ ($1.3 \leqslant x \leqslant 2.2$) phases with the $BaAl_4$-type structure
Andriy V. Tkachuk and Arthur Mar
Page 2298

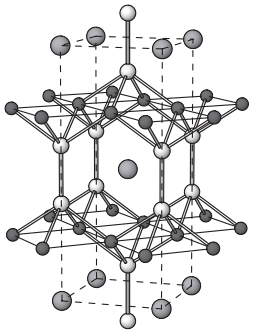

$BaAl_4$-type structure of solid solutions $SrAu_xIn_{4-x}$ ($0.5 \leqslant x \leqslant 1.2$) and $SrAu_xSn_{4-x}$ ($1.3 \leqslant x \leqslant 2.2$), with apical sites preferentially occupied by Au atoms.

Crystal structure and structural disorder of $(Ba_{0.65}Ca_{0.35})_2SiO_4$
Koichiro Fukuda, Masamichi Ito and Tomoyuki Iwata
Page 2305

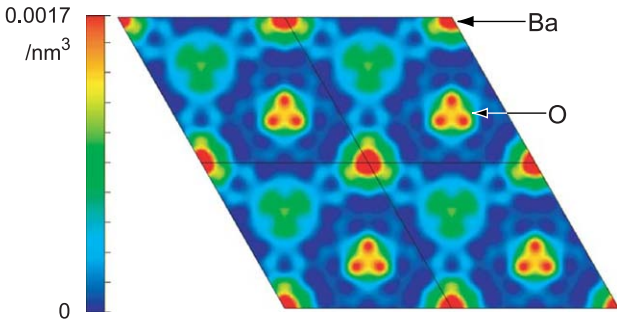

Two-dimensional electron density distribution map showing positional disorder of oxygen atoms.

Study of Ti^{4+} substitution in ZrW_2O_8 negative thermal expansion materials

Klaartje De Buysser, Isabel Van Driessche, Bart Vande Putte, Joseph Schaubroeck and Serge Hoste

Page 2310

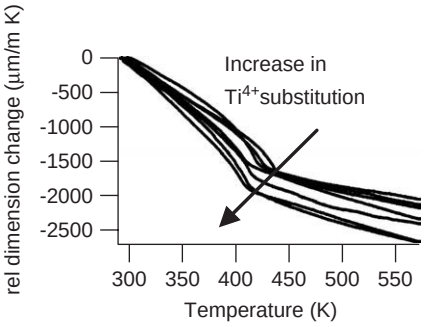

This study indicates that the phase transition temperature in our materials $Zr_{1-x}Ti_xW_2O_8$ is strongly influenced by the bond dissociation energy of the substituting ion–oxygen bond. A decrease in bond strength may compensate for the effect of a decrease in lattice-free volume, lowering the phase transition temperature.

Studies on $InFeMO_4$ (M = Mg, Co, Ni, Cu and Zn) compounds: Crystal structure and cation distribution

M. Matvejeff, J. Lindén, M. Karppinen and H. Yamauchi

Page 2316

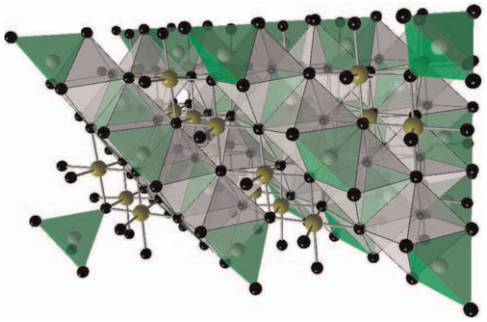

The crystal structure and the cation distribution in a series of $InFeMO_4$ compounds (M = Mg, Co, Ni, Cu and Zn) have been studied by means of X-ray powder diffraction and ^{57}Fe Mössbauer spectroscopy.

$(Mn_{1-x}Pb_x)Pb_{10+y}Sb_{12-y}S_{26-y}Cl_{4+y}O$, a new oxy-chloro-sulfide with ~2 nm-spaced (Mn,Pb)Cl_4 single chains within a waffle-type crystal structure

Charlotte Doussier, Yves Moëlo, Philippe Léone and Alain Meerschaut

Page 2323

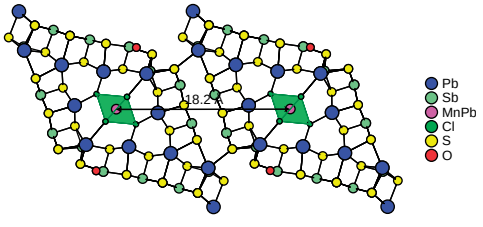

Projection of the crystal structure of $(Mn_{1-x}Pb_x)Pb_{10+y}Sb_{12-y}S_{26-y}Cl_{4+y}O$ restricted to two adjacent rods, showing the minimum distance between (Mn, Pb)Cl_4 single chains.

Epitaxial growth of AlN films on single-crystalline Ta substrates

S. Hirata, K. Okamoto, S. Inoue, T-W. Kim, J. Ohta, H. Fujioka and M. Oshima

Page 2335

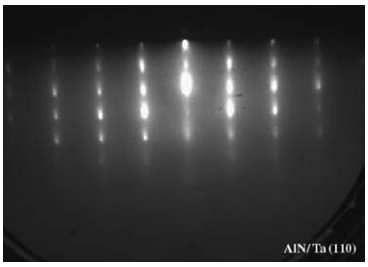

An epitaxial AlN(0001) film with an in-plane epitaxial relationship of AlN[11$\bar{2}$0]//Ta[001] has been obtained for the first time on a Ta(110) substrate by the use of a PLD low-temperature growth technique.

Long Fe_3O_4 nanowires decorated by CdTe quantum dots: Synthesis and magnetic–optical properties

Xianmei Lan, Xuebo Cao, Wenhu Qian, Weijian Gao, Cui Zhao and Yang Guo

Page 2340

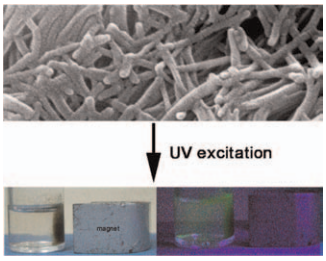

The long and flexible CdTe quantum dots-decorated Fe_3O_4 nanowires assume not only room temperature ferromagnetism but also strong luminescent effect.

The chemistry of the phosphates of barium and tetravalent cations in the 1:1 stoichiometry

Karin Popa, Damien Bregiroux, Rudy J.M. Konings, Thomas Gouder, Aurelian F. Popa, Thorsten Geisler and Philippe E. Raison

Page 2346

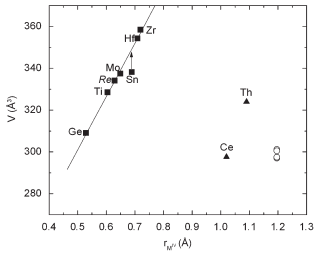

Graphical representation of the variation of the unit-cell volume of $BaM^{IV}(PO_4)_2$ as a function of the ionic radii of M^{IV} cations. Such phosphates crystallise in the $C2/m$ space group for M^{IV} = Ti, Zr, Hf, Ge, Sn, and Mo, and in the $P2_1/n$ space group for $BaTh(PO_4)_2$. The "$BaCe(PO_4)_2$" phosphate previously reported does not exist, as demonstrated in the present paper. Taking into account the present evidence, it can be concluded at this stage that the existence of other Ce(IV) phosphates obtained at high temperature and reported into the literature becomes doubtful.

Continued

Structure, and magnetic and transport behavior of twinned $Ce_2Rh_3(Pb,Bi)_5$

Evan Lyle Thomas, Moo Sung Kim, D.A. Sokolov, Marcus C. Bennett, M.C. Aronson and Julia Y. Chan

Page 2356

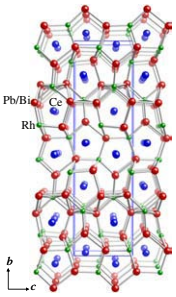

This manuscript reports the crystal growth, structure, and magnetic and transport properties of $Ce_2Rh_3(Pb,Bi)_5$. Magnetization measurements on single crystals find that $Ce_2Rh_3(Pb,Bi)_5$ is a quasi-two-dimensional system, where the Ce moments are spatially well-localized.

Redetermination of the crystal structure of $Ge(HPO_4)_2 \cdot H_2O$, and its thermal behaviour in the range $300 \geqslant T \geqslant 16$ K

Lars Peters and John S.O. Evans

Page 2363

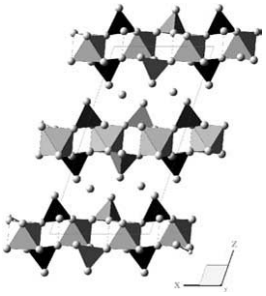

The crystal structure of α-GeP has been redetermined. It is confirmed that α-GeP has α-ZrP type structure. An interpretation for the geometrical trends in α-ZrP type *APTM* is suggested. The thermal behaviour of α-GeP has been from 300 to 16 K. No structural phase transitions have been observed.

Effects of firing schedule on solubility limits and transport properties of ZrO_2–TiO_2–Y_2O_3 fluorites

D.P. Fagg, J.R. Frade, M. Mogensen and J.T.S. Irvine

Page 2371

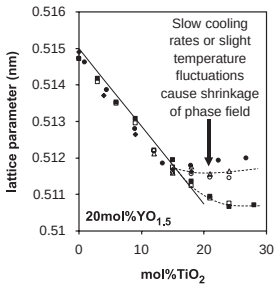

The composition dependence of lattice parameter for compositions containing 20 mol% $YO_{1.5}$ as a function of Ti-content in the system ZrO_2–TiO_2–$YO_{1.5}$ showing contraction of the cubic defect fluorite-phase field upon slight temperature fluctuations or slow cooling rates.

In situ and time resolved study of the γ/α-Fe_2O_3 transition in nanometric particles

T. Belin, N. Millot, N. Bovet and M. Gailhanou

Page 2377

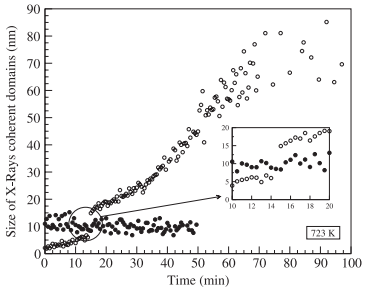

A brutal increase of the X-rays coherent domain sizes of the α-Fe_2O_3 particles during the γ/α transition at nanometric scale. Maghemite γ-Fe_2O_3 particles ($\phi = 9 \pm 1$nm) were heated at 723 K. First germs (or grains) of α-Fe_2O_3 were detected with a size of 2 nm.

Two luminescent frameworks constructed from lead(II) salts with carboxylate ligands containing dinuclear lead(II) units

Xiandong Zhu, Xiaoju Li, Qingyan Liu, Jian Lü, Zhengang Guo, Jinrun He, Yafeng Li and Rong Cao

Page 2386

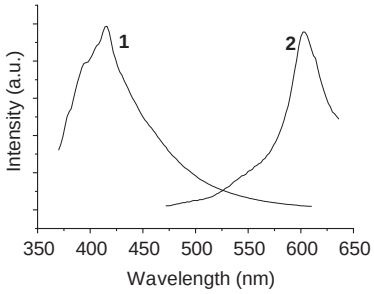

Two luminescent Pb(II) coordination frameworks, $[Pb(PYDC)(H_2O)]_n$ (**1**) and $[Pb(HPHT)]_n$ (**2**) have been prepared. Single-crystal analyses reveal that compound **1** is a three-dimensional architecture consisting of Pb_2O_2 dimeric building units, whereas compound **2** is a two-dimensional layer structure containing one-dimensional lead-oxide chains. The luminescent properties have been investigated, indicating structure-dependent photoluminescent properties of the coordination frameworks.

High-temperature X-ray diffraction and specific heat studies on $GdAlO_3$, $Gd_3Al_5O_{12}$ and $Gd_4Al_2O_9$

Satyajeet Chaudhury, S.C. Parida, K.T. Pillai and K.D. Singh Mudher

Page 2393

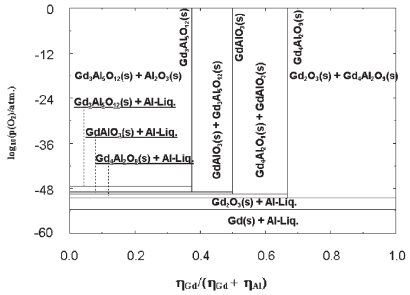

Isothermal oxygen potential diagram for the system Gd–Al–O at 1000 K.

Photoluminescence and structural characteristics of $Lu_2O_3:Eu^{3+}$ nanocrystallites in silica matrix
Jerzy Sokolnicki
Page 2400

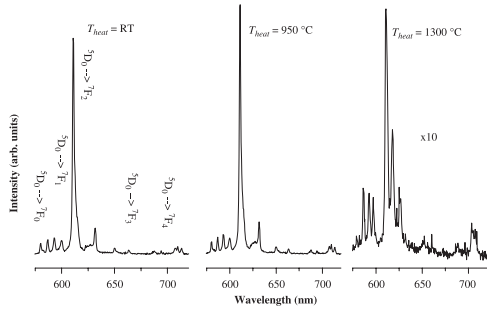

The combination of the solution combustion synthesis and the sol–gel technique allows to obtain a silica ceramic containing nanocrystalline $Lu_2O_3:Eu^{3+}$. The sample treated in temperatures up to 950 °C exhibits almost the same optical properties as compared to nanocrystalline $Lu_2O_3:Eu^{3+}$. The material displays effective red emission under X-ray excitation and no afterglow, and is very promising phosphor for X-ray imaging. At 1300 °C, nanocrystalline $Lu_2O_3:Eu^{3+}$ is converted to lutetium pyrosilicate, $Lu_2Si_2O_7:Eu^{3+}$. Its overall optical performance makes them a good candidate for a cathode-ray phosphor.